Sensors

International Edition: DOI: 10.1002/anie.201909096
German Edition: DOI: 10.1002/ange.201909096

A Dual-Ligand Porous Coordination Polymer Chemiresistor with Modulated Conductivity and Porosity

Ming-Shui Yao, Jia-Jia Zheng, Ai-Qian Wu, Gang Xu, Sanjog S. Nagarkar, Gen Zhang, Masahiko Tsujimoto, Shigeyoshi Sakaki, Satoshi Horike, Kenichi Otake, and Susumu Kitagawa**

Abstract: *Single-ligand-based electronically conductive porous coordination polymers/metal–organic frameworks (EC-PCPs/MOFs) fail to meet the requirements of numerous electronic applications owing to their limited tunability in terms of both conductivity and topology. In this study, a new 2D π-conjugated EC-MOF containing copper units with mixed trigonal ligands was developed: Cu_3(HHTP)(THQ) (HHTP = 2,3,6,7,10,11-hexahydrotriphenylene, THQ = tetrahydroxy-1,4-quinone). The modulated conductivity ($\sigma \approx 2.53 \times 10^{-5}$ S cm^{-1} with an activation energy of 0.30 eV) and high porosity (ca. 441.2 m^2 g^{-1}) of the Cu_3(HHTP)(THQ) semiconductive nanowires provided an appropriate resistance baseline and highly accessible areas for the development of an excellent chemiresistive gas sensor.*

Molecule-based porous compounds, known as metal–organic frameworks (MOFs) or porous coordination polymers (PCPs),[1] have attracted widespread attention for applications such as gas handling and storage,[2] gas separation,[3] and gas sensors.[4] The emergence of electronically conductive MOFs (EC-MOFs), constructed by the periodic connection of metal ions and redox-active organic units,[5] has enabled the long-standing issue to be addressed as to whether conductive stable porous structures can be used for electrical applications.[6] Dozens of EC-MOFs with permanent porosity and conductivity have been developed as semiconductor devices.[7] Among them, two dimensional (2D) π-conjugated EC-MOFs showed exciting semiconductor properties as active materials with satisfactory stability.[4b,6a] The coexistence of crystallinity, porosity, and conductivity creates a platform that can be used for a variety of applications, such as electrocatalysis,[8] supercapacitors,[9] chemiresistive gas sensors,[10] and field-effect transistors (FETs).[11]

However, state-of-the-art 2D π-conjugated EC-MOFs have been limited to systems with a single redox-active organic ligand,[6a,7a] which limits the tunability of both conductivity and topology; thus, it becomes difficult to meet the various requirements for electronic applications. We designed the electronic and porous structure of an EC-MOF by using two types of organic π-conjugated ligands. The use of two ligand types provided us with the ability to create specific properties and functionalities. Typically, 2D π-conjugated EC-MOFs belong to a subclass of hexagonal/tetragonal layered structures and are based on trigonal/square organic ligands and square-planar mononuclear metal nodes.[7a,12] Through selecting the appropriate combination of binary trigonal organic ligands, both "through-bond" pathways in 2D sheets and "through-space" transport between continuously conjugated stacking layers can be modulated, which changes the conductivity and porosity through electron delocalization efficiency and channel shapes, respectively.

Herein, we report that a combination of 2,3,6,7,10,11-hexahydrotriphenylene (HHTP, molecular size, ca. 0.97 nm) ligands in hexagonal $Cu_3(HHTP)_2$[12b] and tetrahydroxy-1,4-quinone (THQ, molecular size, ca. 0.55 nm) ligands in orthorhombic $Cu_3(THQ)_2$[7b] in one material led to a new dual-ligand-based 2D π-conjugated EC-MOF, Cu_3(HHTP)-(THQ) (Figure 1 a). The uniform hybridization of the EC-MOF based on two trigonal organic ligands (containing Cu complexes of two sizes) was expected to generate a unique trigonal crystal structure and ordered arrangement of redox-active ligands on the nanoscale. It was hypothesized that this structure would facilitate improved room-temperature sensing properties in terms of both the electronic properties (low baseline) and surface chemistry (highly accessible surface area). As a proof of concept, the chemiresistive gas-sensing properties of this construct were studied in terms of structure–properties relationships as compared to pristine $Cu_3(HHTP)_2$ at room temperature.

As compared to other reported single-ligand-based 2D π-conjugated EC-MOFs, the square-planar building unit, CuO_4, of Cu_3(HHTP)(THQ) is more complex. This complexity results from the large difference between the two ligands in terms of coordination capability and molecular size. Furthermore, many factors in the synthetic route to Cu_3(HHTP)-(THQ), such as temperature, reaction time, the ratio of HHTP to THQ, and metal salts, were found to dramatically affect the obtained product. All these factors increase the difficulty in controlling the purity, crystallinity, and desired

[*] Dr. M. S. Yao, Prof. J. J. Zheng, S. S. Nagarkar, G. Zhang, M. Tsujimoto, Prof. S. Horike, Prof. K. Otake, Prof. S. Kitagawa
Institute for Integrated Cell-Material Sciences
Kyoto University Institute for Advanced Study, Kyoto University
Yoshida Ushinomiya-cho, Sakyo-ku, Kyoto 606-8501 (Japan)
E-mail: ootake.kenichi.8a@kyoto-u.ac.jp
kitagawa@icems.kyoto-u.ac.jp
A. Q. Wu, Prof. G. Xu
State Key Laboratory of Structural Chemistry, Fujian Institute of Research on the Structure of Matter, Chinese Academy of Sciences
155 Yangqiao Road West, Fuzhou, Fujian, 350002 (P. R. China)
Prof. J. J. Zheng, Prof. S. Sakaki
Fukui Institute for Fundamental Chemistry, Kyoto University
Takano Nishihiraki-cho 34-4, Sakyo-ku, Kyoto 606-8103 (Japan)
Supporting information and the ORCID identification number(s) for the author(s) of this article can be found under: https://doi.org/10.1002/anie.201909096.

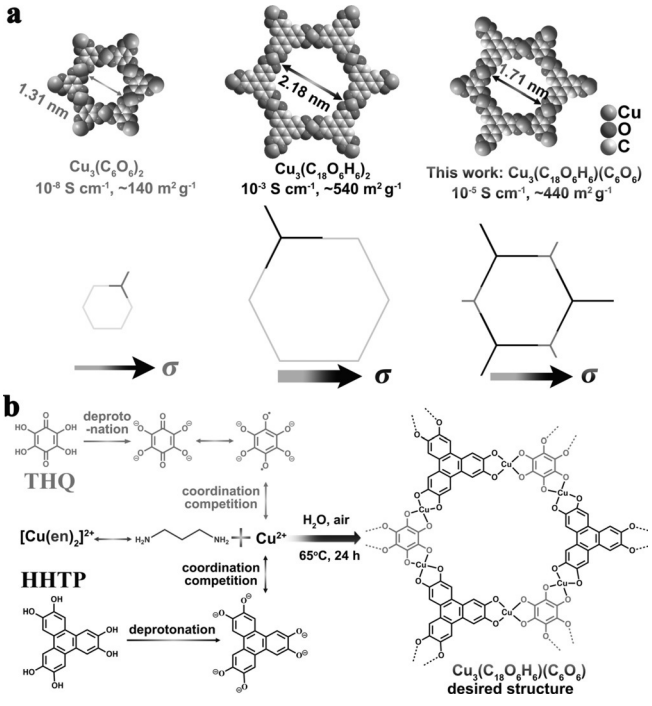

Figure 1. a) Hexagonal structure and properties of $Cu_3(C_{18}O_6H_6)(C_6O_6)$ (expected), $Cu_3(C_6O_6)_2$ (reported), and $Cu_3(C_{18}O_6H_6)_2$ (reported). b) Preparation of the Cu_3(HHTP)(THQ) dual-ligand semiconductor through ethylenediamine-assisted competitive coordination.

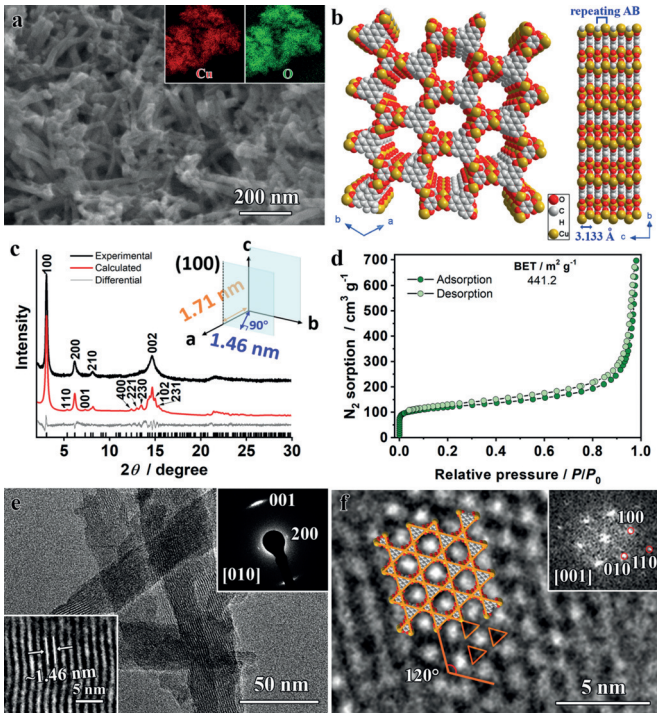

Figure 2. Characterization of Cu_3(HHTP)(THQ). a) SEM image (inset contains EDX mapping images of nanowire bundles). b) Space-filling model of the crystal structure (Cu gold, C gray, O red; hydrogen atoms are omitted for clarity). c) PXRD with Pawley refinement: Observed pattern (black), calculated pattern (red), difference plot (gray), and Bragg positions (black bars). Data were collected at beamline 02B2 in SPring 8, Japan ($\lambda = 0.79962$ Å). Inset describes the calculation of the (100) distance from the trigonal-cell parameters. d) N_2 sorption isotherm. e, f) HRTEM images viewed from the [010] (e) and [001] direction (f). Insets in (e) are the lattice spacing image and SAED pattern; the inset in (f) shows the corresponding FFT analysis.

structure of the final EC-MOF. Experimentally, HHTP shows much stronger coordination with Cu^{2+} than THQ (see Figure S1 in the Supporting Information); thus, crystalline $Cu_3(HHTP)_2$ impurities can readily form during the reaction. Simply increasing the concentration of THQ merely increases the amount of $Cu_3(THQ)_2$ impurities. Therefore, ethylenediamine (en), which can strongly chelate to Cu^{2+} and form the soluble coordination complex $Cu(en)_2$,[7b] was chosen as the base to balance the coordination capability of HHTP and THQ with Cu^{2+} through a competing bond-formation mechanism during the preparation of the Cu_3(HHTP)(THQ) dual-ligand semiconductor (Figure 1; see the Supporting Information for details). The failure to obtain Cu_3(HHTP)(THQ) with monoamine bases also indicates the possible template role of ethylenediamine owing to the suitable length of the spacer in the molecule (see Figures S2 and S3). After optimization of the reaction conditions, pure Cu(HHTP)-(THQ) nanowires were obtained as a crystalline black powder (see Figure S4 and S5).

Figure 2a shows the uniform morphological features of the Cu_3(HHTP)(THQ) nanowires (20–50 nm diameter, hundreds of nanometers long) obtained at 24 h. EDS mapping images clearly reveal the coexistence of Cu and O elements. Together with the simulated crystal structure, synchrotron powder X-ray diffraction (PXRD, $\lambda = 0.79962$ Å) patterns refined by the Pawley method indicated a trigonal unit cell ($P3m1$) with cell parameters of $a = b = 17.154$ Å and $c = 6.266$ Å (Figure 2b,c; see Table S1 in the Supporting Information). The AB slipped-parallel model with slightly slipped stacking of every two layers was energetically favored (see Figure S6). The broad (002) peak at $2\theta = 14.68°$ (28.48° for $\lambda = 1.54178$ Å) indicated short-range ordering along the c-axis as compared with the narrow and sharp (100) peak at $2\theta = 3.08°$ (5.95° for $\lambda = 1.54178$ Å) of the ab plane, which is commonly observed for 2D π-conjugated PCP/MOFs.[6b,7b,12b,13] The N_2 sorption isotherm at 77 K of Cu_3-(HHTP)(THQ) shows a BET surface area of approximately 441.2 m^2 g^{-1} (Figure 2d), thus revealing an intrinsically high porosity that cannot be achieved simply through a nonporous AB stacking structure with 60° rotations between neighboring layers or a significantly slipped parallel structure (see Figures S7 and S8).

High-resolution transmission electron microscopy (HRTEM) and the selected area electron diffraction (SAED) pattern further supports the assertion that the nanowires are growing along the c-axis and show a typical lattice spacing of (100) facets (Figure 2e). A honeycomb structure with a pore size of approximately 1.3–1.4 nm was observed by HRTEM from the c-axis (Figure 2f), and the in-plane periodicity was also evident from the corresponding fast Fourier transform (FFT) analysis (Figure 2f, inset). In contrast to the uniformly distributed ligands of the same size in single-ligand-based $Cu_3(HHTP)_2$,[12b,14] it can be observed in high-resolution areas that three symmetrical, but isolated, black areas corresponding to large HHTP ligands (marked by

three triangles in Figure 2 f) in a honeycomb structure uniformly surround each pore. This arrangement is consistent with the simulated trigonal structure containing uniformly dispersed large HHTP ligands and small THQ ligands. These results also rule out the formation of $Cu_3(HHTP)_{2/3}(THQ)_{4/3}$ and $Cu_3(HHTP)_{4/3}(THQ)_{2/3}$, which would show different pore structures and lattice spacings (see Figure S9).

Elemental analysis (EA) and thermogravimetric analysis/differential thermal analysis (TG/DTA) were used to verify the charge and composition of $Cu_3(HHTP)(THQ)$. The as-prepared sample had a high percentage of N, up to approximately 4.6 wt% (see Tables S2 and S3). We attributed the presence of N to the protonated ethylenediamine ($NH_3CH_2CH_2NH_3^{2+}$) used in the reaction. Bao and co-workers reported similar results, the presence of $[Cu_3(C_6O_6)_2(NH_3CH_2CH_2NH_3)_{1.36}]$, in their study, in which they employed ethylenediamine as a copper-chelating agent.[7b] Ethylenediamine could not be completely removed, even by treatment with hot water or Soxhlet extraction with methanol, possibly because it served as a counterion to neutralize the negatively charged CuO_4 (see Figures S10 and S11).[7b,12b,15] The corresponding EA results suggested a chemical formula of $[Cu_3(C_{18}O_6H_6)(C_6O_6)(H_2O)_{11.78}(NH_3CH_2CH_2NH_3)_{1.59}]$ for $Cu_3(HHTP)(THQ)$ (see Table S2). In combination with calculations using positively charged protonated ethylenediamine ($1.59\times2/3$), the results indicated that each square-planar CuO_4 center in the $Cu_3(HHTP)(THQ)$ framework was negatively charged (−1).

To further confirm the composition and study the thermal stability of $Cu_3(HHTP)(THQ)$, we examined the as-synthesized product by TG/DTA. The mass-loss value of guest molecules (ca. 20.4%; calcd: 21.5% for loss of H_2O) before about 200 °C and total mass loss of approximately 42.3% at 500 °C (calcd: 47.4% mass loss for the final products of copper–carbon mixtures) was consistent with the EA-deduced formula (see Table S2 and Figure S12). Good thermal stability, up to approximately 300 °C in N_2 and 180 °C in air, was also observed (see Figure S13). The temperature-dependent PXRD patterns in air further confirmed the good thermal stability of $Cu_3(HHTP)(THQ)$ crystals (Figure 3 a). This result indicates the strong potential for the application of such materials in various electronic devices that must operate over a broad temperature range.

We performed conductivity measurements to investigate the electronic properties of $Cu_3(HHTP)(THQ)$ (Figure 3 b,c). The linear and zero drift of the temperature-dependent *I–V* curves indicate good ohmic contact between the $Cu_3(HHTP)(THQ)$ pellets and the Pt electrodes (two-probe method; Figure 3 b). To avoid the influence of humidity and other interfering gases, this experiment was performed in an argon-filled glove box. The increase in conductivity (σ) with increasing temperature revealed the semiconducting behavior of the $Cu_3(HHTP)(THQ)$ powder pellet. A semiconductivity value of approximately $2.53\times10^{-5}\,S\,cm^{-1}$ was observed, which was slightly higher than that in air with 35% relative humidity (ca. $5\times10^{-6}\,S\,cm^{-1}$), and between those of $Cu_3(THQ)_2$ (ca. $10^{-8}\,S\,cm^{-1}$) and $Cu_3(HHTP)_2$ (ca. $10^{-3}\,S\,cm^{-1}$).[7b,10a] Similarly, a medium thermal activation energy of 0.30 eV was estimated from the linear fitting of $\log\sigma$ versus $1/T$ (Figure 3 c; $Cu_3(HHTP)_2$: 0.16 eV, $Cu_3(THQ)_2$: 0.46 eV).[7b,10a] Figure 3 d shows the current versus time plots of the $Cu_3(HHTP)(THQ)$ powder pellet as obtained by the DC reverse polarity method ($-x$V was applied first on the pellet, and then the polarity was quickly reversed to $+x$V; $x=$ 1, 2, 3, 4, and 5).[16] For all curves ranging from 1 to 5 V, the lagging ionic current peak was not observed. Thus, ions are not the dominant charge carrier, and $Cu_3(HHTP)(THQ)$ was confirmed to be the electronically conductive material.

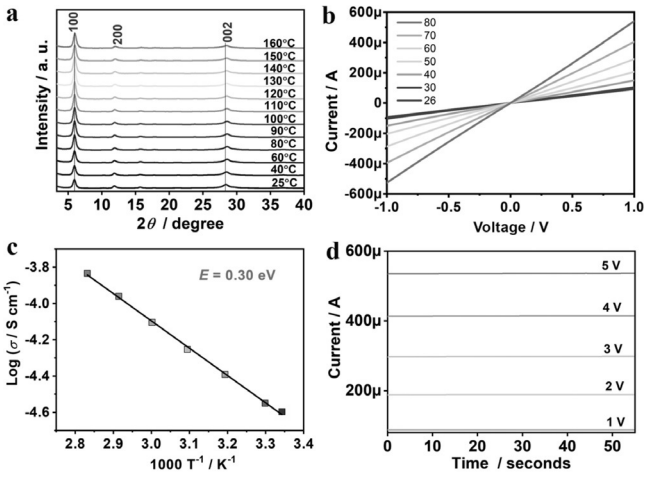

Figure 3. a) Temperature-dependent PXRD patterns of $Cu_3(HHTP)(THQ)$ in air. b, c) Temperature-dependent *I–V* curves (b) and $\log\sigma$ versus T^{-1} plot (c) of a $Cu_3(HHTP)(THQ)$ powder pellet in Ar (two-probe method). d) Curves of current versus time obtained by the DC reverse polarity method.

The semiconductivity and low activation energy indicated that $Cu_3(HHTP)(THQ)$ might possess room-temperature gas-sensing properties. Accordingly, $Cu_3(HHTP)(THQ)$ nanowires were used as the active material of a room-temperature chemiresistive gas sensor (Figure 4). The sensing measurements were conducted using a home-made dynamic sensing setup (see the Supporting Information for details).[10a,17] The gas sensors based on a $Cu_3(HHTP)(THQ)$ nanowire thick film were fabricated on insulating substrates with predeposited Au interdigital electrodes by the drop-coating method followed by activation under flowing dry air at room temperature. The dynamic sensing curves of the $Cu_3(HHTP)(THQ)$ sensor over a broad range of NH_3 concentrations (1 ppm to saturated vapor) showed good response–recovery properties at room temperature (the response and recovery times were 1.65 and 2.57 min, respectively, toward 10 ppm NH_3; Figure 4 a; see also Figures S14 and S15). Notably, the sensor showed good discrimination of NH_3 in the low concentration range (1–100 ppm). This capability has yet to be demonstrated for sensors based on $Cu_3(HHTP)_2$, $Cu_3(HITP)_2$, and $Ni_3(HITP)_2$ powders[10,13] and might be due to the successful decrease in the conductivity baseline of the active sensing material (by about two orders of magnitude as compared with single-ligand-based EC-MOFs), thus enabling greater sensitivity to small charge transfers caused by low-concentration gas adsorption.

The good linear log–log plots of response versus concentration (Figure 4 b) are consistent with typical chemiresistive

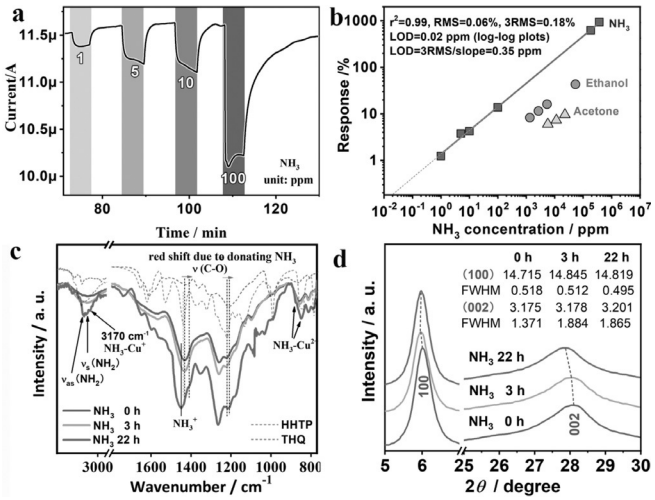

Figure 4. Room-temperature gas-sensing performance of the thick-film gas sensor based on Cu_3(HHTP)(THQ) nanowires. a) Response–recovery curve toward NH_3 at different concentrations. b) Response–concentration log–log plot for NH_3 (plots for ethanol and acetone are also shown, in which case their concentration is shown on the *x*-axis). c) IR spectra and d) PXRD patterns before and after exposure to NH_3.

behavior. The theoretical limit of detection (LOD) was calculated to be approximately 0.02 ppm using the linear log–log plot and approximately 0.35 ppm using the linear plot by setting the response equal to 3 RMS (RMS = root-mean-square deviation).[12a,18] These values are comparable with the lowest LOD values of room-temperature chemiresistors reported to date (see Table S4). When compared with common interfering gases, such as ethanol and acetone, the sensor also showed good selectivity toward NH_3 (Figure 4b; see also Figures S16 and S17). The good selectivity toward NH_3 might be due to the strong gas–framework interaction, as revealed by the IR peaks of NH_3–Cu^+ and NH_3–Cu^{2+}, and the resulting red shift of υ(C–O) (Figure 4c).[19] This strong interaction was further confirmed by the lattice expansion observed upon NH_3 adsorption by PXRD (Figure 4d). Such expansion was not observed with O_2 because there are only weak interactions between O_2 and the framework (see Figure S18).

In summary, a new 2D π-conjugated dual-ligand-based EC-MOF, Cu_3(HHTP)(THQ), was synthesized by a simple solution-phase method. This EC-MOF possessed a unique trigonal crystal structure and modulated conductivity. The obtained crystalline black powders of Cu_3(HHTP)(THQ) nanowires indicated a trigonal unit cell (P3 m1) with cell parameters of $a = b = 17.154$ and $c = 6.266$ Å in an AB slightly slipped parallel stacking mode. The products not only showed modulated conductivity (ca. 2.53×10^{-5} S cm^{-1}) and semiconductive behavior with a thermal activation energy of 0.30 eV, but also exhibited high porosity (ca. 441.2 m^2 g^{-1}). A Cu_3(HHTP)(THQ) nanowire thick-film sensor exhibited good discrimination toward low concentrations of NH_3 with an excellent LOD as low as 0.02–0.35 ppm. The dual-ligand based EC-MOFs provided a new design for the modulation of electronic conductivity and porosity. We trust this work will inspire the design of more dual- or multi-ligand-based EC-MOFs containing unique combinations organic ligands with different sizes, shapes, or functional groups for the discovery of new functional materials.

Acknowledgements

This study was supported by KAKENHI Grants-in-Aid for Specially Promoted Research (JP25000007), Scientific Research (S) (JP18H05262), and Early-Career Scientists (JP19K15584) from the Japan Society for the Promotion of Science (JSPS), an International Research Fellowship of the JSPS (Postdoctoral Fellowships for Research in Japan (Standard), P18334), the National Natural Science Foundation of China (21801243, 21822109), and the Natural Science Foundation of Fujian Province (2019J01129). We thank Mika Gochomori at iCeMS, Kyoto University, for her contributions to organic ligand synthesis, and Dr. Mickaele Bonneau, Dr. Ping Wang, Dr. Yi-Fan Gu, and Dr. Lavenn Christophe at iCeMS, Kyoto University, for their contributions to materials characterization.

Conflict of interest

The authors declare no conflict of interest.

Keywords: gas sensors · metal–organic frameworks · nanowires · porous coordination polymers · semiconductors

How to cite: *Angew. Chem. Int. Ed.* **2020**, *59*, 172–176
Angew. Chem. **2020**, *132*, 178–182

[1] a) N. Hosono, A. Terashima, S. Kusaka, R. Matsuda, S. Kitagawa, *Nat. Chem.* **2019**, *11*, 109–116; b) L. Heinke, C. Wöll, *Adv.* **2019**, *31*, 1806324; c) J. Liu, J. Ye, Z. Li, K.-i. Otake, Y. Liao, A. W. Peters, H. Noh, D. G. Truhlar, L. Gagliardi, C. J. Cramer, O. K. Farha, J. T. Hupp, *J. Am. Chem. Soc.* **2018**, *140*, 11174–11178.

[2] a) M. Ding, R. W. Flaig, H.-L. Jiang, O. M. Yaghi, *Chem. Soc. Rev.* **2019**, *48*, 2783–2828; b) S. Bhattacharya, W. W. Ayass, D. H. Taffa, A. Schneemann, A. L. Semrau, S. Wannapaiboon, P. J. Altmann, A. Pöthig, T. Nisar, T. Balster, N. C. Burtch, V. Wagner, R. A. Fischer, M. Wark, U. Kortz, *J. Am. Chem. Soc.* **2019**, *141*, 3385–3389.

[3] a) C. Gu, N. Hosono, J.-J. Zheng, Y. Sato, S. Kusaka, S. Sakaki, S. Kitagawa, *Science* **2019**, *363*, 387–391; b) L. Li, R.-B. Lin, R. Krishna, H. Li, S. Xiang, H. Wu, J. Li, W. Zhou, B. Chen, *Science* **2018**, *362*, 443–446; c) G. Lal, M. Derakhshandeh, F. Akhtar, D. M. Spasyuk, J.-B. Lin, M. Trifkovic, G. K. Shimizu, *J. Am. Chem. Soc.* **2019**, *141*, 1045–1053.

[4] a) M. L. Aubrey, M. T. Kapelewski, J. F. Melville, J. Oktawiec, D. Presti, L. Gagliardi, J. R. Long, *J. Am. Chem. Soc.* **2019**, *141*, 5005–5013; b) Z. Meng, R. M. Stolz, L. Mendecki, K. A. Mirica, *Chem. Rev.* **2019**, *119*, 478–598.

[5] a) T. Kambe, R. Sakamoto, K. Hoshiko, K. Takada, M. Miyachi, J.-H. Ryu, S. Sasaki, J. Kim, K. Nakazato, M. Takata, H. Nishihara, *J. Am. Chem. Soc.* **2013**, *135*, 2462–2465; b) A. J. Clough, J. M. Skelton, C. A. Downes, A. A. De La Rosa, J. W. Yoo, A. Walsh, B. C. Melot, S. C. Marinescu, *J. Am. Chem. Soc.* **2017**, *139*, 10863–10867.

[6] a) W.-T. Koo, J.-S. Jang, I.-D. Kim, *Chem* **2019**, *5*, 1938–1963; b) R. Dong, P. Han, H. Arora, M. Ballabio, M. Karakus, Z.

Zhang, C. Shekhar, P. Adler, P. S. Petkov, A. Erbe, *Nat. Mater.* **2018**, *17*, 1027.
[7] a) L. Sun, M. G. Campbell, M. Dincă, *Angew. Chem. Int. Ed.* **2016**, *55*, 3566 – 3579; *Angew. Chem.* **2016**, *128*, 3628 – 3642; b) J. Park, A. C. Hinckley, Z. Huang, D. Feng, A. A. Yakovenko, M. Lee, S. Chen, X. Zou, Z. Bao, *J. Am. Chem. Soc.* **2018**, *140*, 14533 – 14537.
[8] E. M. Miner, T. Fukushima, D. Sheberla, L. Sun, Y. Surendranath, M. Dincă, *Nat. Commun.* **2016**, *7*, 10942.
[9] a) D. Sheberla, J. C. Bachman, J. S. Elias, C. J. Sun, Y. Shao-Horn, M. Dinca, *Nat. Mater.* **2017**, *16*, 220 – 224; b) D. Feng, T. Lei, M. R. Lukatskaya, J. Park, Z. Huang, M. Lee, L. Shaw, S. Chen, A. A. Yakovenko, A. Kulkarni, *Nat. Energy* **2018**, *3*, 30.
[10] a) M.-S. Yao, X.-J. Lv, Z.-H. Fu, W.-H. Li, W.-H. Deng, G.-D. Wu, G. Xu, *Angew. Chem. Int. Ed.* **2017**, *56*, 16510 – 16514; *Angew. Chem.* **2017**, *129*, 16737 – 16741; b) M. G. Campbell, D. Sheberla, S. F. Liu, T. M. Swager, M. Dincă, *Angew. Chem. Int. Ed.* **2015**, *54*, 4349 – 4352; *Angew. Chem.* **2015**, *127*, 4423 – 4426.
[11] G. Wu, J. Huang, Y. Zang, J. He, G. Xu, *J. Am. Chem. Soc.* **2017**, *139*, 1360 – 1363.
[12] a) Z. Meng, A. Aykanat, K. A. Mirica, *J. Am. Chem. Soc.* **2019**, *141*, 2046 – 2053; b) M. Hmadeh, Z. Lu, Z. Liu, F. Gándara, H. Furukawa, S. Wan, V. Augustyn, R. Chang, L. Liao, F. Zhou, E. Perre, V. Ozolins, K. Suenaga, X. Duan, B. Dunn, Y. Yamamto, O. Terasaki, O. M. Yaghi, *Chem.* **2012**, *24*, 3511 – 3513.
[13] M. G. Campbell, S. F. Liu, T. M. Swager, M. Dincă, *J. Am. Chem. Soc.* **2015**, *137*, 13780 – 13783.
[14] W. H. Li, K. Ding, H. R. Tian, M. S. Yao, B. Nath, W. H. Deng, Y. Wang, G. Xu, *Adv. Funct. Mater.* **2017**, *27*, 1702067.
[15] L. E. Darago, M. L. Aubrey, C. J. Yu, M. I. Gonzalez, J. R. Long, *J. Am. Chem. Soc.* **2015**, *137*, 15703 – 15711.
[16] a) J. Huang, Y. He, M.-S. Yao, J. He, G. Xu, M. Zeller, Z. Xu, *J. Mater. Chem. A* **2017**, *5*, 16139 – 16143; b) K. Jiang, T. Fei, F. Jiang, G. Wang, T. Zhang, *Sens. Actuators B* **2014**, *192*, 658 – 663.
[17] M. S. Yao, W. X. Tang, G. E. Wang, B. Nath, G. Xu, *Adv. Mater.* **2016**, *28*, 5229 – 5234.
[18] a) J. Li, Y. Lu, Q. Ye, M. Cinke, J. Han, M. Meyyappan, *Nano Lett.* **2003**, *3*, 929 – 933; b) S. Ammu, V. Dua, S. R. Agnihotra, S. P. Surwade, A. Phulgirkar, S. Patel, S. K. Manohar, *J. Am. Chem. Soc.* **2012**, *134*, 4553 – 4556.
[19] a) T. Yu, T. Hao, D. Fan, J. Wang, M. Shen, W. Li, *J. Phys. Chem. C* **2014**, *118*, 6565 – 6575; b) L. Ma, Y. Cheng, G. Cavataio, R. W. McCabe, L. Fu, J. Li, *Appl. Catal. B* **2014**, *156*, 428 – 437.

Manuscript received: July 21, 2019
Accepted manuscript online: October 8, 2019
Version of record online: November 22, 2019

